

Designing Extremely Low-Power Topological Transistors with 1T'-MoS₂ and HZO for Cryogenic Applications

Yosep Park^a, Yungyeong Park^b, Hyeonseok Choi^b, Subeen Lim^b, and Yeonghun Lee^{a,b,c}*

^aDepartment of Intelligent Semiconductor Engineering, Incheon National University, 119
Academy-ro, Yeonsu-gu, Incheon 22012, Republic of Korea

^bDepartment of Electronics Engineering, Incheon National University, Incheon National
University, 119 Academy-ro, Yeonsu-gu, Incheon 22012, Republic of Korea

^cResearch Institute for Engineering and Technology, Incheon National University, 119
Academy-ro, Yeonsu-gu, Incheon 22012, Republic of Korea

*Email: y.lee@inu.ac.kr

ABSTRACT : Large-scale quantum computing requires cryogenic electronic controllers such as control/readout circuit and routing circuit. However, current technologies face high power dissipation problems, hindering large-scale qubit integration. Here, we theoretically propose extremely low-power cryogenic topological transistors, i.e., negative-capacitance topological insulator field-effect transistors (NC-TIFETs). By combining a gate-field-induced two-dimensional 1T'-Molybdenum Disulfide (MoS_2) topological channel with a Hafnium–Zirconium Oxide (HZO) ferroelectric gate insulator, NC-TIFETs exhibit an extremely steep-slope transfer curve and ultra-high transconductance at low drain voltage (V_D). Therefore, NC-TIFETs are the compelling candidate for minimizing power dissipation in the cryogenic electronic interfaces essential for large-scale quantum computing systems.

KEYWORDS : Topological insulators, Negative capacitance, 1T'- MoS_2 , HZO, Steep-slope switching, Ultra-high transconductance

Researchers have been developed quantum computers to solve complex problems that classical computers cannot solve¹⁻³. To enable large-scale quantum computing systems, electronic controllers (i.e., control/readout circuits and routing circuits) that can minimize the number of coaxial cables to operating quantum computing systems (Figure 1a)⁴⁻⁸. However, as qubit scalability increases, these controllers are faced with the challenge of consuming power that exceeds the cooling power limits available in conventional dilution refrigerators^{3,9,10}. In order to resolve the cooling power problems, III-V high-electron-mobility transistors (HEMTs) have been investigated for their potential of low-power dissipation and high-frequency operation^{7,8,11-13}. Nevertheless, the power dissipation of HEMTs has remained too high for operating large-scale

quantum computing systems^{9,10,14}. To overcome the power consumption bottleneck in electronic controllers, we propose extremely low-power transistors based on a novel operational principle, utilizing two-dimensional topological insulators (2D TIs). 2D TIs offer two key advantages: their topologically protected edge states enable ballistic transport by suppressing backscattering, and they undergo a topological phase transition from the quantum spin Hall (QSH) to the normal insulator (NI) phase as an out-of-plane electric field (E_z) breaks inversion symmetry^{15,16}. The properties of these 2D TIs make them applicable as TIFETs, characterized by novel switching mechanisms and high on-state currents.

In addition to the aforementioned properties, the TIFET possesses a desirable character that can maximize the gain of NC operation that ferroelectric materials introduce. In conventional FETs, the quantum capacitance (C_Q) formed at the onset of inversion is known to cause undesirable hysteresis in the I_D - V_G characteristics, thereby limiting the gain from the NC effect¹⁷. In contrast, during the switching operation of TIFETs, only the edge states are modulated while there are no charges in most part (i.e., bulk) of the TIs. Accordingly, such inversion in FETs does not occur during the TIFET operation, which allows us to take full advantage of the NC to amplify the electric field in the TIFETs. Although the conceptual framework of NC-TIFET has been proposed previously¹⁸, our work provides comprehensive analyses including current-voltage characteristics and discusses superior performance in the context of large-scale quantum computers.

In this work, we theoretically propose a device model for the NC-TIFET by combining the tight-binding (TB) model¹⁹, $\mathbf{k} \cdot \mathbf{p}$ model^{20,21}, non-equilibrium Green's function (NEGF) formalisms^{22,23}, and incorporating the NC effects via Landau-Khalatnikov (L-K) equation²⁴. Our model provides a theoretical analysis for achieving steep-slope switching and maximizing the E_z amplification through the incorporation of ferroelectric materials. Subsequently, the voltage gain (A_V) of the

NC-TIFET is compared to that of a conventional negative capacitance field-effect transistor (NCFET), analyzing the differences in A_V in the context of their equivalent capacitance circuits and charge modulation characteristics. Finally, the simulation results demonstrated that NC-TIFETs exhibit an extremely steep-slope transfer curve compared with typical TIFETs. Additionally, the steep-slope transfer curve results in ultra-high transconductance (g_m) at low V_D , thereby maximizing its potential for cryogenic applications in quantum computing electronic controllers, such as control, readout, and routing circuits.

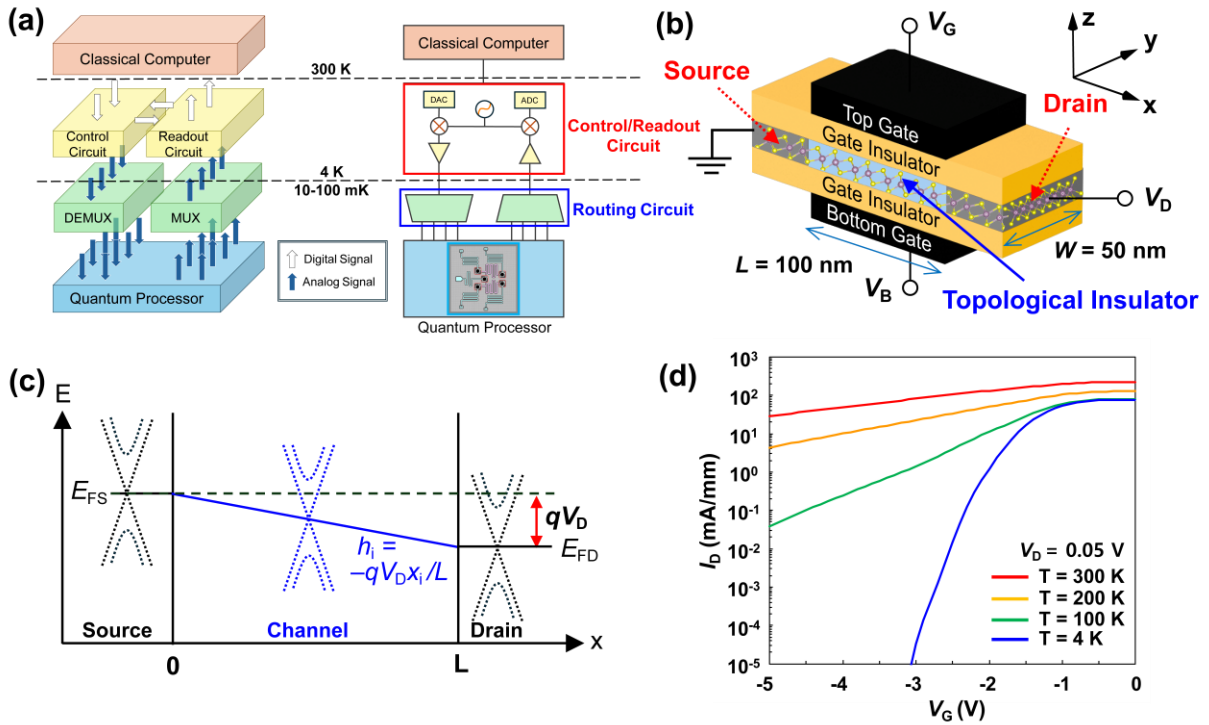


Figure 1. Conceptual architecture of a large-scale quantum computing system and TIFET device characteristics. (a) Schematic of large-scale quantum computing architecture and its distinct temperature stages. The quantum processor and routing circuits (MUX/DEMUX) operate at 10–100 mK, the control/readout circuits at 4 K, and the classical computer at room temperature (300 K). Digital and analog signal paths are indicated. (b) Device structure of double-gate TIFETs.

The channel consists of a 1T'-MoS₂ topological insulator (TI). Gate insulator consists of dielectric layer (in TIFETs) or ferroelectric materials (in NC-TIFETs). (c) The energy band diagram in real space along the channel direction with E - k band structures for the on-state. E_{FS} and E_{FD} represent the Fermi level in the source and the drain, respectively, with an applied drain voltage qV_D . (d) Transfer characteristics (I_D - V_G) of the TIFET with a 1T'-MoS₂ channel, swept from $T = 4$ K to 300 K at fixed drain voltage $V_D = 0.05$ V.

The TIFET comprises a double-gate structure with a nanoribbon channel constructed by a topological insulator (TI), integrated with source and drain terminals. The TI channel is sandwiched by gate insulators—a dielectric layer for a TIFET or a ferroelectric layer for an NC-TIFET—and is controlled by top (V_G) and bottom (V_B) gates. (Figure 1b) The device has a channel length (L) of 100 nm and a channel width (W) of 50 nm, where parameters are optimized for avoiding tunneling leakage and finite size effect (Figure S1 of Supporting Information 5). We selected 1T'-MoS₂ as the channel material due to its low critical field (E_c)²⁰, which enables rapid topological phase transitions for ON-OFF modulation. The parameters used for the TIFET model are outlined in the Supporting Information 1 and 2.

For the TIFET to operate, the E_z for ON-OFF state modulation and the V_D for driving the current are essential. Figure 1c illustrates the energy band diagram of the TIFET under an applied V_D . Due to the applied V_D , the channel potential is assumed to vary linearly along the channel, creating a difference between the source and drain Fermi levels (E_{FS} and E_{FD} , respectively). This potential difference, defined as $E_{FS} = E_{FD} + qV_D$, drives a drain current governed by quantum conductance. To implement this linear potential drop in our model, we add onsite energy term $h_i = -\frac{qV_D x_i}{L}$, where q is elementary charge, x_i is the position of site i from the source to drain region. Figure 1d

shows the I_D - V_G of the TIFET at various temperatures ranging from 4 K to 300 K, with $V_D = 0.05$ V. Due to its ballistic edge-state transport, the TIFET enables a high on-state current governed by quantum conductance. At room temperature (300K), the device performance is severely degraded. The small bandgap of 1T'-MoS₂ (45–47 meV)^{20,21}, allows thermally excited carriers to create a leakage path, bypassing gate control and resulting in a poor on/off ratio of approximately 10 (at $V_G = -5$ V). At cryogenic temperatures, however, this thermal leakage path is strongly suppressed. As seen in Figure 1d, cooling the device to 4 K dramatically improves the on/off ratio, highlighting that while the TIFET is unsuitable for room-temperature logic, its high switching performance is maximized in cryogenic environments.

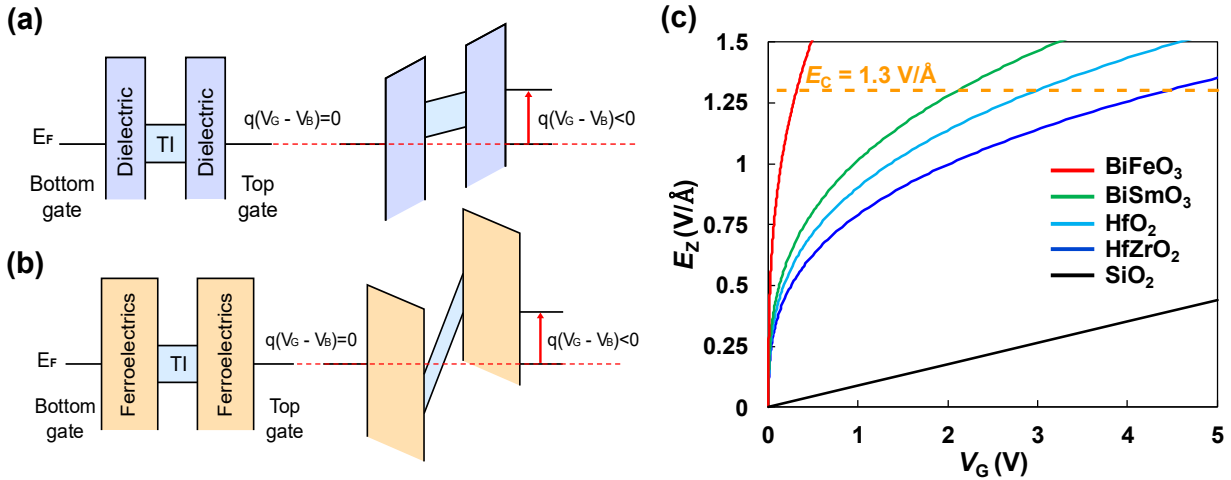


Figure 2. Mechanism of electric field amplification in NC-TIFETs. Energy band diagram of (a) a TIFET with a dielectric insulator layer and (b) an NC-TIFET with a ferroelectric insulator. The diagrams illustrate the state at zero gate bias ($q(V_G - V_B) = 0$ V, left) and under an applied gate bias ($q(V_G - V_B) < 0$ V), respectively. (c) The E_z as a function of V_G with a 1T'-MoS₂ channel, using various gate insulators : BiFeO₃²⁵, BiSmO₃²⁶, HfO₂²⁷, HfZrO₂²⁸, and SiO₂ (0.5 nm

thickness). The dashed orange line indicates the E_c point, required to the topological phase transition.

The E_z amplification mechanism of TIFETs, which depends on the gate insulator type, is illustrated in Figure 2a-b. When the gate bias is not applied, TIFETs maintain their topological phase, characterized by the presence of topological edge states. Conversely, when a gate bias is applied to TIFETs with a dielectric insulator layer, a limited E_z is obtained due to the voltage drop across the insulator. In contrast, the NC-TIFET utilizes the NC effects of a ferroelectric layer to generate internal voltage amplification, inducing a substantially larger E_z in the channel for the same V_G .

The L-K equation, which describes the polarization (P) and electric field in a ferroelectric material (E_{FE}), is given by

$$E_{FE} = 2\alpha_{FE}P + 4\beta_{FE}P^3. \quad (1)$$

Where α_{FE} and β_{FE} are the ferroelectric material parameters. The device operates under a voltage division condition, $V_G = V_{FE}(E_z) + \psi_s$, where V_{FE} and ψ_s are the voltages across the ferroelectric layer and the surface potential of TI channel, respectively. The detail derivation of V_{FE} is documented in the Supporting Information 4. Figure 2c shows the E_z as a function of V_G for effects by various gate insulators. Notably, this relationship of V_G makes maximum electric field amplification condition, when ferroelectric material thickness $t_{FE} = 1/(2\alpha_{FE}C_{ch})$, where C_{ch} is channel capacitance. Within the optimized t_{FE} , maximum gate voltage condition ($V_{G,max}$) is calculated as

$$V_{G,max} = \frac{C_{ch}^2 t_{ch}^3}{P_F^2} E_z^3. \quad (2)$$

Where t_{ch} is channel thickness, and P_{r} is remanent polarization of the ferroelectric material, which P_{r} is equal to $P_{\text{r,max}}$ in NC-TIFETs condition.

This equation provides a powerful design principle: a higher P_{r} dramatically reduces the gate voltage required to switch the device. As predicted by Eq. (2), bismuth iron oxide^{25,29} (BiFeO₃, BFO), with its exceptionally high P_{r} , is capable of reaching the E_{c} at an ultra-low V_{G} . However, BFO presents a critical manufacturing challenge: its NC performance is acutely sensitive to the t_{FE} and deviating from the optimal thickness leads to a loss of amplification or undesirable hysteresis (see Figure S3 of the Supporting Information). Therefore, we selected HZO²⁸ as the gate insulator. HZO is a hafnium-based dielectric employed in contemporary semiconductor devices, ensuring its compatibility with existing manufacturing processes³⁰. Crucially, HZO is compatible with atomic layer deposition (ALD), which represents a superior engineering conformality, large-area uniformity, and atomic level thickness control³¹. We expect that utilizing of ALD for the fabrication of HZO leads to optimized t_{FE} , thereby achieving stable, hysteresis-free NC operation.

Our HZO ferroelectric parameters used in this study are based on room-temperature values²⁸. At cryogenic temperatures, however, the coercive field (E_{co}) typically increases, which can shift the optimized t_{FE} and the hysteresis window. To address this, we systematically investigate the impact of E_{co} variations on the t_{FE} optimization and the hysteresis window in the Supporting Information 7 (Figure S3 and S4). Furthermore, the impact of P_{r} on switching characteristics is demonstrated in Figure S6 of Supporting Information.

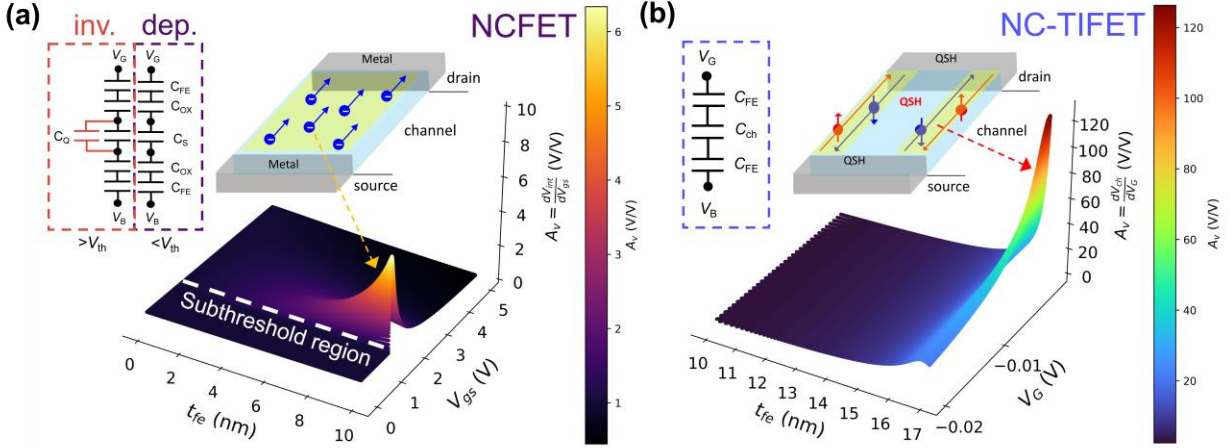


Figure 3. Comparison of voltage gains A_V between an NCFET and an NC-TIFET. (a) The voltage gain ($A_V = dV_{\text{int}}/dV_{\text{GS}}$) of the NCFET with a Si channel and an HZO ferroelectric layer, plotted as a function of t_{FE} and gate-source voltage (V_{GS}). The subthreshold region is indicated by the white dashed line. (b) The voltage gain ($A_V = dV_{\text{ch}}/dV_{\text{G}}$) of the NC-TIFET with a 1T'-MoS₂ channel and an HZO ferroelectric layer, is shown as a function of t_{FE} and V_{G} . Insets for each device depict the equivalent capacitance circuit (top-left) and a schematic of device operation (center). 2D cross-sectional plots Gain vs V_{G} are provided in Figure S5 of Supporting Information.

NCFETs have been considered promising candidates for future low-power applications due to their ability to achieve sub-60 mV/dec SS, which is attributed to the polarization response of the ferroelectric material that amplifies the gate voltage^{30,32,33}. However, NCFETs are known that have critical hysteresis issue, if the capacitance matching process is not correctly performed¹⁷. The main element of hysteresis is the C_Q , which increases rapidly after bulk charge inversion, mainly occur in modern FETs with ultra-thin channels. (see equivalent capacitance circuit in Figure 3a). Therefore, even if capacitance matching is achieved to minimize hysteresis, the A_V induced by NC is significantly limited in the sub-threshold region due to the limited availability of charges in the gate stack to promote voltage growth (see Figure 3a). In contrast, NC-TIFETs modulate only the

edge states during switching, thereby avoiding charge generation within the bulk. In other words, unlike NCFETs, NC-TIFETs exhibit a channel behavior similar to that of a dielectric material, meaning that the channel capacitance is largely independent of the gate bias. This characteristic leads to a series capacitance circuit that is primarily influenced by the ferroelectric capacitance and the channel capacitance (see equivalent capacitance circuit in Figure 3b). As a result, NC-TIFETs can achieve hysteresis-free operation under optimal t_{FE} conditions, which allows for the realization of maximum A_V values.

While TIFETs avoid the C_Q bottleneck via the absence of bulk inversion, the topological edge states introduce a finite C_Q at the edges. Crucially, these edge states are robust features protected by the bulk band topology. As a result, the edge C_Q is expected to be negligible with respect to the inversion-symmetry breaking in the bulk, while the topologically protected edges ensure stable transport. To accurately model the electrostatics including edge states, it is essential to employ rigorous two-dimensional electrostatic simulations that account for the parallel geometric contributions of the conducting edges and the insulating bulk under vertical electric gate fields. Consequently, we identify the precise quantification of edge C_Q and its impact on capacitance scaling as a subject for future investigation.

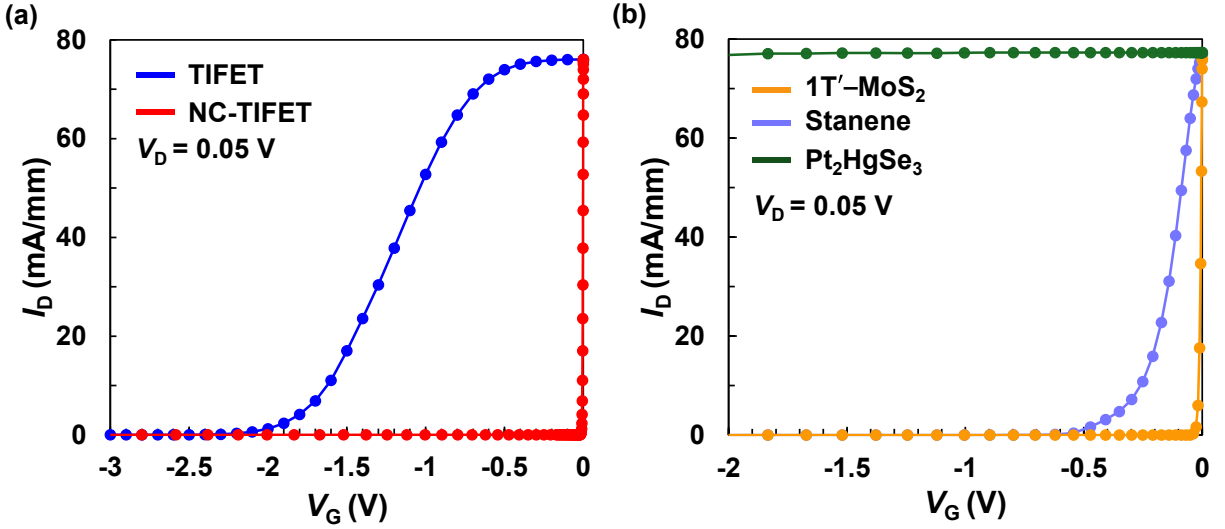


Figure 4. Transfer characteristics and the effect of various topological channel materials. (a) Comparison of transfer characteristics for a conventional TIFET (blue) and an NC-TIFET (red) at $V_D = 0.05$ V. Both devices utilize a $1T'$ -MoS₂ channel. (b) Transfer characteristics of NC-TIFETs using three different topological channel materials: $1T'$ -MoS₂, stanene, and Pt₂HgSe₃. The ferroelectric gate is HZO for all devices.

Due to the superior A_V in NC-TIFETs, NC-TIFETs can result in an extremely steep-slope transfer curve. TIFETs require a large switching voltage to induce a topological phase transition, because of positive voltage drop of dielectric material when induced gate bias (see Figure 2a). In contrast, the negative voltage drop in NC layer and hysteresis-free operation of the NC-TIFET allows to a dramatically steepened transfer curve (Figure 4a), and powerful output characteristics (see Figure S7 of supporting information). Next, we investigated the role of the channel material on device performance by comparing three different 2D topological insulators: $1T'$ -MoS₂^{20,21}, stanene¹⁹, and Pt₂HgSe₃^{34,35} (Figure 4b). Stanene has been identified as a promising 2D TI material due to its small band gap and a large material-specific parameter that influences the E_c ¹⁹. However, NC-TIFETs based on stanene channel material result in a switching voltage of approximately 0.5 V,

offering no significant power dissipation advantage over conventional HEMTs. Pt_2HgSe_3 has also been identified as a promising 2D TI material, because of large band gap to prevent thermal leakage. However, Pt_2HgSe_3 of large band gap (160 meV³⁴) and relatively low electric field potential parameter (i.e., α_V and α_R , see Table S2 of supporting information.) impedes the device from switching OFF within extremely low voltage range. In contrast, due to small band gap and high material specific parameter effecting for E_z ²¹ (see Table S1 of supporting information.), 1T'-MoS₂ get ultra-low switching voltage, (see Figure 5) which emerges as a strong candidate for cryogenic applications. The model parameters for these topological materials are provided in Figure S2 of the Supporting Information.

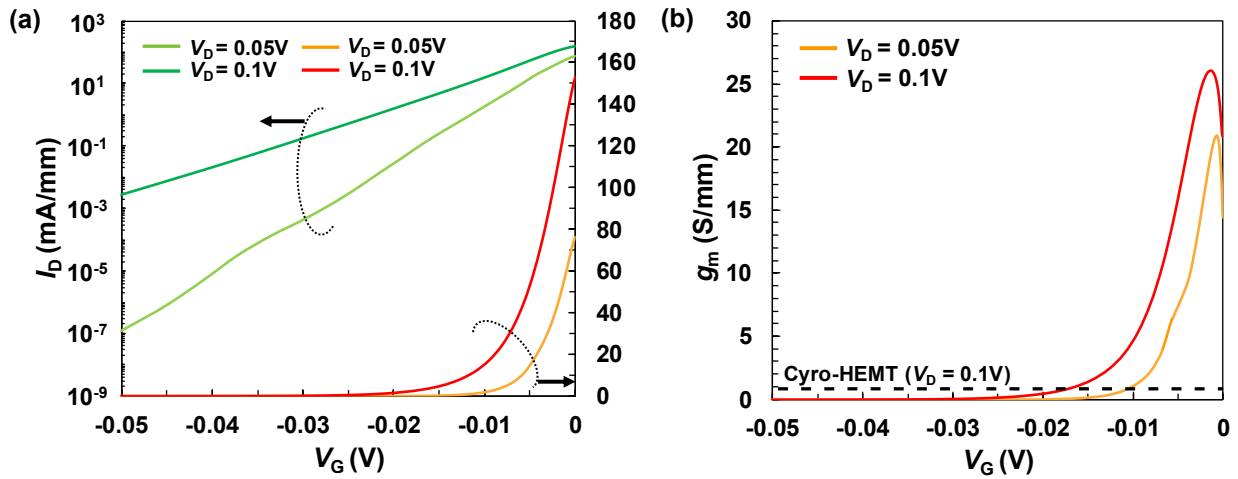


Figure 5. Electrical characteristics of NC-TIFETs. (a) Transfer characteristics ($I_D - V_G$) of the TIFET and NC-TIFET at $V_D = 0.05\text{ V}$ and 0.1 V . (b) Transconductance characteristics ($g_m - V_G$) at $V_D = 0.05\text{ V}$ and 0.1 V , benchmarked against experimental data from a Cryo-HEMT⁸. All of data were obtained at $T = 4\text{K}$. For all results shown in Figure 5, the channel and ferroelectric materials are 1T'-MoS₂ and HZO, respectively.

As the result, the optimized combination of 1T'-MoS₂ and HZO Combination results in an extremely steep-slope transfer curve. As shown in Figure 5a, the NC-TIFET achieves a sub-20 mV switching voltage (defined for an ON/OFF ratio of 10³) even at a low drain bias of $V_D = 0.05$ V. Notably, despite this low operating V_D , rapid switching capability of NC-TIFETs produces an exceptionally high g_m of approximately 26 S/mm at $V_D = 0.1$ V. This value is over an order of magnitude higher than the experimentally recorded g_m of a state-of-the-art Cryo-HEMT (0.8 S/mm)⁸ (Figure 5b). It is important to acknowledge that the experimental Cryo-HEMT data reflect parasitic effects and non-idealities—such as interface traps and gate leakage—which inevitably degrade g_m , whereas our model captures the intrinsic performance limits. However, even after accounting for these extrinsic factors, the combination of an ultra-low switching voltage and high transconductance establishes the NC-TIFET as a compelling candidate for cryogenic electronic interfaces, including low-noise amplifiers (LNAs) and analog-to-digital converters (ADCs).

While the presented NC-TIFET, modeled with DFT-derived parameters, demonstrates exceptional performance, it is important to note that this represents an idealized case. Therefore, in order for the development of such technology to proceed, it is necessary that several fundamental issues be identified and addressed at the structural, device, and contact levels. First, at the structural level, stack engineering should be explored. While our single-layer ferroelectric design demonstrates excellent switching, the integration of multi-layer stacks has emerged as a promising strategy to enhance ON-currents and decreased gate capacitance. Second, to validate the device's potential for analog applications such as amplifiers, a thorough analysis of its high-frequency (RF) and noise characteristics is imperative. To this end, it is imperative to incorporate the effects of parasitic capacitance within the TIFET, necessitating the precise calculation of the transit frequency (f_T), power consumption (P_{DC}), and noise indication factor is important. Especially, conventional noise

indication factor for charge-based devices such as HEMTs (i.e., the $\sqrt{I_D}g_m^{-1}$ factor^{8,36}) may not be directly applicable due to the characteristics of spin current based topological edge states. Therefore, a novel noise model may be necessary, incorporating unique spin-based transport and realistic impurity scattering mechanisms, including magnetic impurities at the edge states^{37,38}. Third, for practical circuit applications such as LNAs or DACs/ADCs, realizing complementary p-type characteristics is essential. Although realistic modeling of p-type TIFETs remains unexplored, we suggest that p-type operation could be theoretically achieved by inverting the double-gate bias configuration (i.e., swapping the roles of the top and bottom gate voltages). This inversion enables p-type modulation without physical doping. However, further research is required to fully elucidate the operational mechanisms of p-type TIFETs and develop specific integration schemes for CMOS architectures. Finally, the practical implementation of the source/drain (S/D) contacts warrants discussion. While our theoretical model assumes ideal contacts where the S/D regions are integrated with the same topological channel, the physical interface is critical for effectively exploiting topological edge states. We propose two viable approaches: (1) phase engineering, utilizing 1T-1T' heterostructures as demonstrated in recent 1T-2H heterophase studies^{39,41}, where the metallic phase 1T can effectively decrease R_C and enhance device current^{40,41}. (2) One-dimensional (1D) edge contacts, which have been proposed as a key solution for reducing the contact resistance^{42,43}. Furthermore, our analytical model incorporating finite R_C (Supporting Information 10) confirms that the NC gain remains robust, preserving steep switching characteristics even under realistic contact conditions (Figure S8). Therefore, overcoming these multilevel will be crucial for realizing the full potential of NC-TIFETs as high-performance cryogenic devices for large-scale quantum computing systems. In conclusion, we have theoretically demonstrated that the NC-TIFET architecture overcomes the fundamental

quantum capacitance bottleneck of NCFETs, enabling superior switching performance by fully exploiting the NC effect. As a result, our device achieves superior switching characteristics, including a sub-20 mV switching voltage (at $V_D = 0.05$ V) and an ultra-high transconductance of 26 S/mm (at $V_D = 0.1$ V), establishing the NC-TIFET as a key technology for the cryogenic electronic interfaces for large-scale quantum computing, such as LNAs and ADCs.—However, while gate-tunable 1T'-MoS₂ has been experimentally observed⁴⁴, translating these theoretical advantages into reality requires addressing the metastability of the 1T'-MoS₂ phase^{45,46,47,48}. Future efforts must focus on robust fabrication strategies—such as surface passivation^{49,50}, control of magnetic impurities in edge states^{37,38}, and defect engineering⁵⁰—to stabilize the 1T' phase against NC-induced high internal fields and ensure reliable operation. Consequently, establishing a stable fabrication process for 1T'-MoS₂ remains the critical milestone for realizing high-performance NC-TIFETs in large-scale cryogenic quantum computing systems.

ASSOCIATED CONTENT

Supporting Information

The Supporting Information is available free of charge at

<https://pubs.acs.org/doi/10.1021/acs.nanolett.5c06182>.

Device parameters, model method in NC-TIFETs, DFT parameters of 1T'-MoS₂, Pt₂HgSe₃, and stanene, L–K equation used to model NC-TIFETs, optimization of the NC-TIFET channel length and width, model parameter fitting for DFT, optimization of the ferroelectric thickness (t_{FE}) in NC-TIFETs in cryogenic environments, effects of different ferroelectric materials in NC-TIFETs, output characteristics of NC-TIFETs, and formulas for the TIFET drain current equation combined with contact resistance (PDF)

AUTHOR INFORMATION

Corresponding Author

Yeonghun Lee - Department of Intelligent Semiconductor Engineering, Incheon National University, 119 Academy-ro, Yeonsu-gu, Incheon 22012, Republic of Korea; Department of Electronics Engineering, Incheon National University, Incheon National University, 119 Academy-ro, Yeonsu-gu, Incheon 22012, Republic of Korea; Research Institute for Engineering and Technology, Incheon National University, 119 Academy-ro, Yeonsu-gu, Incheon 22012, Republic of Korea; orcid.org/0000-0002-6058-1316; Email: y.lee@inu.ac.kr

Authors

Yosep Park - Department of Intelligent Semiconductor Engineering, Incheon National University, 119 Academy-ro, Yeonsu-gu, Incheon 22012, Republic of Korea; orcid.org/0009-0003-0123-8942

Yungyeong Park - Department of Electronics Engineering, Incheon National University, Incheon National University, 119 Academy-ro, Yeonsu-gu, Incheon 22012, Republic of Korea; orcid.org/0009-0008-6621-4796

Hyeonseok Choi - Department of Electronics Engineering, Incheon National University, Incheon National University, 119 Academy-ro, Yeonsu-gu, Incheon 22012, Republic of Korea; orcid.org/0009-0006-1523-5605

Subeen Lim - Department of Electronics Engineering, Incheon National University, Incheon National University, 119 Academy-ro, Yeonsu-gu, Incheon 22012, Republic of Korea; orcid.org/0009-0002-1957-2677

Complete contact information is available at:

<https://pubs.acs.org/10.1021/acs.nanolett.5c06182>

Author Contributions

Y.L. supervised the projects. Yo.P., Yu.P., H.C., and S.L. performed the theoretical calculation and data analysis. Yo.P., Yu.P., and Y.L. wrote the manuscript. All authors have discussed the results, read the manuscript, and agreed with its content.

Notes

The authors declare the following competing financial interest(s): Yo.P., Yu.P., and Y.L. hold two Korean patents (Field Effect Transistor Using Phase Transition Channel Material; and Apparatus and System for Quantum Computing Including Quantum Transistor) related to the technology described in this work.

ACKNOWLEDGMENT

This work was supported by the National Research Foundation of Korea (NRF) grant funded by the Korea government (MSIT) (No. 2022R1F1A1073068).

Reference

- (1) Arute, F.; Arya, K.; Babbush, R.; Bacon, D.; Bardin, J. C.; Barends, R.; Biswas, R.; Boixo, S.; Brandao, F. G. S. L.; Buell, D. A.; Burkett, B.; Chen, Y.; Chen, Z.; Chiaro, B.; Collins, R.; Courtney, W.; Dunsworth, A.; Farhi, E.; Foxen, B.; Fowler, A.; Gidney, C.; Giustina, M.; Graff, R.; Guerin, K.; Habegger, S.; Harrigan, M. P.; Hartmann, M. J.; Ho, A.; Hoffmann, M.; Huang, T.; Humble, T. S.; Isakov, S. V.; Jeffrey, E.; Jiang, Z.; Kafri, D.; Kechedzhi, K.; Kelly, J.; Klimov, P. V.; Knysh, S.; Korotkov, A.; Kostritsa, F.; Landhuis, D.; Lindmark, M.; Lucero, E.; Lyakh, D.; Mandrà, S.; McClean, J. R.; McEwen, M.; Megrant, A.; Mi, X.; Michielsen, K.; Mohseni, M.; Mutus, J.; Naaman, O.; Neeley, M.; Neill, C.; Niu, M. Y.; Ostby, E.; Petukhov, A.; Platt, J. C.; Quintana, C.; Rieffel, E. G.; Roushan, P.; Rubin, N. C.; Sank, D.; Satzinger, K. J.; Smelyanskiy, V.; Sung, K. J.; Trevithick, M. D.; Vainsencher, A.; Villalonga, B.; White, T.; Yao, Z. J.; Yeh, P.; Zalcman, A.; Neven, H.; Martinis, J. M. Quantum Supremacy Using a Programmable Superconducting Processor. *Nature* **2019**, *574* (7779), 505–510. <https://doi.org/10.1038/s41586-019-1666-5>.
- (2) Kim, Y.; Eddins, A.; Anand, S.; Wei, K. X.; van den Berg, E.; Rosenblatt, S.; Nayfeh, H.; Wu, Y.; Zaletel, M.; Temme, K.; Kandala, A. Evidence for the Utility of Quantum Computing

- before Fault Tolerance. *Nature* **2023**, *618* (7965), 500–505. <https://doi.org/10.1038/s41586-023-06096-3>.
- (3) Ferraris, A.; Cha, E.; Mueller, P.; Moselund, K.; Zota, C. B. Cryogenic Quantum Computer Control Signal Generation Using High-Electron-Mobility Transistors. *Commun Eng* **2024**, *3* (1), 1–7. <https://doi.org/10.1038/s44172-024-00293-2>.
 - (4) Charbon, E.; Sebastiano, F.; Vladimirescu, A.; Homulle, H.; Visser, S.; Song, L.; Incandela, R. M. Cryo-CMOS for Quantum Computing. In *2016 IEEE International Electron Devices Meeting (IEDM)*; 2016; p 13.5.1-13.5.4. <https://doi.org/10.1109/IEDM.2016.7838410>.
 - (5) Sebastiano, F.; van Dijk, J. P. G.; Hart, P. A. 't; Patra, B.; van Staveren, J.; Xue, X.; Almudever, C. G.; Scappucci, G.; Veldhorst, M.; Vandersypen, L. M. K.; Vladimirescu, A.; Pellerano, S.; Babaie, M.; Charbon, E. Cryo-CMOS Interfaces for Large-Scale Quantum Computers. In *2020 IEEE International Electron Devices Meeting (IEDM)*; 2020; p 25.2.1-25.2.4. <https://doi.org/10.1109/IEDM13553.2020.9372075>.
 - (6) Pauka, S. J.; Das, K.; Kalra, R.; Moini, A.; Yang, Y.; Trainer, M.; Bousquet, A.; Cantaloube, C.; Dick, N.; Gardner, G. C.; Manfra, M. J.; Reilly, D. J. A Cryogenic CMOS Chip for Generating Control Signals for Multiple Qubits. *Nat Electron* **2021**, *4* (1), 64–70. <https://doi.org/10.1038/s41928-020-00528-y>.
 - (7) Jeong, J.; Kim, S. K.; Kim, J.; Lee, J.; Kim, J. P.; Kim, B. H.; Suh, Y.-J.; Geum, D.-M.; Park, S.-Y.; Kim, S. 3D Stackable Cryogenic InGaAs HEMT-Based DC and RF Multiplexer/Demultiplexer for Large-Scale Quantum Computing. In *2022 International Electron Devices Meeting (IEDM)*; 2022; p 4.5.1-4.5.4. <https://doi.org/10.1109/IEDM45625.2022.10019363>.
 - (8) Jeong, J.; Kim, S. K.; Suh, Y.-J.; Lee, J.; Choi, J.; Kim, J. P.; Kim, B. H.; Park, J.; Shim, J.; Rheem, N.; Lee, C. J.; Jo, Y.; Geum, D.-M.; Park, S.-Y.; Kim, J.; Kim, S. Cryogenic III-V and Nb Electronics Integrated on Silicon for Large-Scale Quantum Computing Platforms. *Nat Commun* **2024**, *15* (1), 10809. <https://doi.org/10.1038/s41467-024-55077-1>.
 - (9) Agashiwala, K.; Pal, A.; Cui, H.; Chavan, T.; Cao, W.; Banerjee, K. Advancing High-Performance Large-Scale Quantum Computing with Cryogenic 2D-CMOS. In *2023 International Electron Devices Meeting (IEDM)*; 2023; pp 1–4. <https://doi.org/10.1109/IEDM45741.2023.10413702>.
 - (10) Ferraris, A.; Cha, E.; Mueller, P.; Morf, T.; Prathapan, M.; Sousa, M.; Han, H.-C.; Enz, C.; Zota, C. B. Cryogenic InGaAs HEMT-Based Switches For Quantum Signal Routing. In *2022 International Electron Devices Meeting (IEDM)*; 2022; p 4.6.1-4.6.4. <https://doi.org/10.1109/IEDM45625.2022.10019536>.
 - (11) Jeong, J.; Kwang Kim, S.; Kim, J.; Geum, D.-M.; Lee, J.; Park, S.-Y.; Kim, S. 3D Stackable Cryogenic InGaAs HEMTs for Heterogeneous and Monolithic 3D Integrated Highly Scalable Quantum Computing Systems. In *2022 IEEE Symposium on VLSI Technology and Circuits (VLSI Technology and Circuits)*; 2022; pp 328–329. <https://doi.org/10.1109/VLSITechnologyandCir46769.2022.9830449>.
 - (12) Cha, E.; Wadefalk, N.; Moschetti, G.; Pourkabirian, A.; Stenarson, J.; Grahn, J. InP HEMTs for Sub-mW Cryogenic Low-Noise Amplifiers. *IEEE Electron Device Letters* **2020**, *41* (7), 1005–1008. <https://doi.org/10.1109/LED.2020.3000071>.
 - (13) Yoo, J.-H.; Jeon, Y.-S.; Son, S.-W.; Lee, I.-G.; Jo, H.-B.; Choi, S.-M.; Yu, M.-S.; Park, W.-S.; Kim, H.-J.; Lee, H.-J.; Son, S.-P.; Kim, S.K.; Yun, J.; Shim, J.-P.; Jang, H.; Lee, K.; Jeong, Y.; Kim, T.; Shin, C.-S.; Kim, T.-W.; Lee, J.-H.; Seo, K.-S.; Yang, K.; Kim, D.-H. Single-Power-Supply Compatible Cryogenic In_{0.8}Ga_{0.2}As Quantum-Well HEMTs with

- Record Combination of High-Frequency and Low-Noise Performance for Quantum-Computing Applications. In *2024 IEEE Symposium on VLSI Technology and Circuits (VLSI Technology and Circuits)*; 2024; pp 1–2. <https://doi.org/10.1109/VLSITechnologyandCir46783.2024.10631365>.
- (14) Reilly, D. J. Challenges in Scaling-up the Control Interface of a Quantum Computer. In *2019 IEEE International Electron Devices Meeting (IEDM)*; 2019; p 31.7.1-31.7.6. <https://doi.org/10.1109/IEDM19573.2019.8993497>.
- (15) Kane, C. L.; Mele, E. J. Quantum Spin Hall Effect in Graphene. *Phys. Rev. Lett.* **2005**, *95* (22), 226801. <https://doi.org/10.1103/PhysRevLett.95.226801>.
- (16) Kane, C. L.; Mele, E. J. Z₂ Topological Order and the Quantum Spin Hall Effect. *Phys. Rev. Lett.* **2005**, *95* (14), 146802. <https://doi.org/10.1103/PhysRevLett.95.146802>.
- (17) Cao, W.; Banerjee, K. Is Negative Capacitance FET a Steep-Slope Logic Switch? *Nature Communications* **2020**, *11* (1), 196. <https://doi.org/10.1038/s41467-019-13797-9>.
- (18) Fuhrer, M. S.; Edmonds, M. T.; Culcer, D.; Nadeem, M.; Wang, X.; Medhekar, N.; Yin, Y.; Cole, J. H. Proposal for a Negative Capacitance Topological Quantum Field-Effect Transistor. In *2021 IEEE International Electron Devices Meeting (IEDM)*; 2021; p 38.2.1-38.2.4. <https://doi.org/10.1109/IEDM19574.2021.9720587>.
- (19) Park, Y., Park, H., Choi, S., Lim, D., Kim, Y. & Lee, Y. Tight-Binding Device Modeling of 2-D Topological Insulator Field-Effect Transistors with Gate-Induced Phase Transition. *IEEE Trans. Electron Devices* **71**, 5739–5743 (2024). <https://doi.org/10.1109/Ted.2024.3427091>.
- (20) Qian, X.; Liu, J.; Fu, L.; Li, J. Quantum Spin Hall Effect in Two-Dimensional Transition Metal Dichalcogenides. *Science* **2014**, *346* (6215), 1344–1347. <https://doi.org/10.1126/science.1256815>.
- (21) Das, B.; Sen, D.; Mahapatra, S. Tuneable Quantum Spin Hall States in Confined 1T' Transition Metal Dichalcogenides. *Sci Rep* **2020**, *10* (1), 6670. <https://doi.org/10.1038/s41598-020-63450-5>.
- (22) Keldysh, L. V. Diagram Technique for Nonequilibrium Processes. In *Selected Papers of Leonid V Keldysh*; WORLD SCIENTIFIC, 2023; pp 47–55. https://doi.org/10.1142/9789811279461_0007.
- (23) Datta, S. Electrical Resistance: An Atomistic View. *Nanotechnology* **2004**, *15* (7), S433. <https://doi.org/10.1088/0957-4484/15/7/051>.
- (24) L. D., L.; I. M., K. On the Anomalous Absorption of Sound near a Second Order Phase Transition Point. *Dokl. Akad. Nauk SSSR* **1954**, *96* (469), 25.
- (25) Zhang, J. X.; He, Q.; Trassin, M.; Luo, W.; Yi, D.; Rossell, M. D.; Yu, P.; You, L.; Wang, C. H.; Kuo, C. Y.; Heron, J. T.; Hu, Z.; Zeches, R. J.; Lin, H. J.; Tanaka, A.; Chen, C. T.; Tjeng, L. H.; Chu, Y.-H.; Ramesh, R. Microscopic Origin of the Giant Ferroelectric Polarization in Tetragonal-like BiFeO_3 . *Phys. Rev. Lett.* **2011**, *107* (14), 147602. <https://doi.org/10.1103/PhysRevLett.107.147602>.
- (26) Yang, Q.; Hu, J.; Fang, Y.-W.; Jia, Y.; Yang, R.; Deng, S.; Lu, Y.; Dieguez, O.; Fan, L.; Zheng, D.; Zhang, X.; Dong, Y.; Luo, Z.; Wang, Z.; Wang, H.; Sui, M.; Xing, X.; Chen, J.; Tian, J.; Zhang, L. Ferroelectricity in Layered Bismuth Oxide down to 1 Nanometer. *Science* **2023**, *379* (6638), 1218–1224. <https://doi.org/10.1126/science.abm5134>.
- (27) Schenk, T.; Fancher, C. M.; Park, M. H.; Richter, C.; Künneth, C.; Kersch, A.; Jones, J. L.; Mikolajick, T.; Schroeder, U. On the Origin of the Large Remanent Polarization in La:HfO₂.

- (28) Zacharaki, C.; Tsipas, P.; Chaitoglou, S.; Fragkos, S.; Axiotis, M.; Lagoyiannis, A.; Negrea, R.; Pintilie, L.; Dimoulas, A. Very Large Remanent Polarization in Ferroelectric Hf_{1-x}Zr_xO₂ Grown on Ge Substrates by Plasma Assisted Atomic Oxygen Deposition. *Appl. Phys. Lett.* **2019**, *114* (11), 112901. <https://doi.org/10.1063/1.5090036>.
- (29) You, L.; Abdelsamie, A.; Zhou, Y.; Chang, L.; Lim, Z. S.; Wang, J. Revisiting the Ferroelectric Photovoltaic Properties of Vertical BiFeO₃ Capacitors: A Comprehensive Study. *ACS Appl. Mater. Interfaces* **2023**, *15* (9), 12070–12077. <https://doi.org/10.1021/acsami.2c23023>.
- (30) Jung, M.; Kim, H.-B.; Park, Y.; Park, J.; Lee, H.; Oh, S.; Kim, K. K.; Ahn, J.-H.; Lee, Y.; Na, J.; Suh, D. High-Performance Negative Capacitance Field-Effect Transistors with Synthetic Monolayer MoS₂. *ACS Nano* **2025**, *19* (18), 17503–17513. <https://doi.org/10.1021/acsnano.4c18973>.
- (31) Trinh, N. L.; Gu, B.; Yang, K.; Nguyen, C. T.; Lee, B.; Kim, H.-M.; Kim, H.; Kang, Y.; Park, M. H.; Lee, H.-B.-R. Atomic-Level Stoichiometry Control of Ferroelectric Hf_xZr_yO_z Thin Films by Understanding Molecular-Level Chemical Physical Reactions. *ACS Nano* **2025**, *19* (3), 3562–3578. <https://doi.org/10.1021/acsnano.4c13595>.
- (32) You, W.-X.; Su, P. Intrinsic Difference Between 2-D Negative-Capacitance FETs With Semiconductor-on-Insulator and Double-Gate Structures. *IEEE Transactions on Electron Devices* **2018**, *65* (10), 4196–4201. <https://doi.org/10.1109/TED.2018.2866125>.
- (33) Park, Y.; Lee, H.; Lee, Y. Trap-Enhanced Steep-Slope Negative-Capacitance FETs Using Amorphous Oxide Semiconductors. *ACS Appl. Electron. Mater.* **2025**, *7* (12), 5705–5711. <https://doi.org/10.1021/acsaelm.5c00767>.
- (34) Bafekry, A.; Stampfl, C.; Nguyen, C.; Ghergherehchi, M.; Mortazavi, B. Tunable Electronic Properties of the Dynamically Stable Layered Mineral Pt₂HgSe₃ (Jacutingaite). *Phys. Chem. Chem. Phys.* **2020**, *22* (42), 24471–24479. <https://doi.org/10.1039/D0CP04388E>.
- (35) Kandrai, K.; Vancsó, P.; Kukucska, G.; Koltai, J.; Baranka, G.; Ákos Hoffmann; Áron Pekker; Kamarás, K.; Horváth, Z. E.; Vymazalová, A.; Tapasztó, L.; Nemes-Incze, P. Signature of Large-Gap Quantum Spin Hall State in the Layered Mineral Jacutingaite. *Nano Lett.* **2020**, *20* (7), 5207–5213. <https://doi.org/10.1021/acsnanolett.0c01499>.
- (36) Pospieszalski, M. W. Extremely Low-Noise Amplification with Cryogenic FETs and HFETs: 1970-2004. *IEEE Microwave Magazine* **2005**, *6* (3), 62–75. <https://doi.org/10.1109/MMW.2005.1511915>.
- (37) Jelver, L. Spontaneous Breaking of Time-Reversal Symmetry at the Edges of $T\text{-Mo}$ Monolayer Transition Metal Dichalcogenides. *Phys. Rev. B* **2019**, *99* (15). <https://doi.org/10.1103/PhysRevB.99.155420>.
- (38) Jäck, B.; Xie, Y.; Bernevig, B. A.; Yazdani, A. Observation of Backscattering Induced by Magnetism in a Topological Edge State. *Proceedings of the National Academy of Sciences* **2020**, *117* (28), 16214–16218. <https://doi.org/10.1073/pnas.2005071117>.
- (39) Wang, S.; Zhang, D.; Li, B.; Zhang, C.; Du, Z.; Yin, H.; Bi, X.; Yang, S. Ultrastable In-Plane 1T–2H MoS₂ Heterostructures for Enhanced Hydrogen Evolution Reaction. *Advanced Energy Materials* **2018**, *8* (25), 1801345. <https://doi.org/10.1002/aenm.201801345>.

- (40) Kappera, R.; Voiry, D.; Yalcin, S. E.; Branch, B.; Gupta, G.; Mohite, A. D.; Chhowalla, M. Phase-Engineered Low-Resistance Contacts for Ultrathin MoS₂ Transistors. *Nature Mater* **2014**, *13* (12), 1128–1134. <https://doi.org/10.1038/nmat4080>.
- (41) Lin, Y.; Lee, H.; Kang, J.; Wang, Z.; Haasch, R. T.; Chyczewski, S. T.; Liu, Z.; Chuang, H.-C.; Zheng, J.-F.; Zhu, W. Single-Step Synthesis of In-Plane 1T'-2H Heterophase MoTe₂ for Low-Resistance Contacts. *Advanced Functional Materials* n/a (n/a), e11589. <https://doi.org/10.1002/adfm.202511589>.
- (42) Wang, L.; Meric, I.; Huang, P. Y.; Gao, Q.; Gao, Y.; Tran, H.; Taniguchi, T.; Watanabe, K.; Campos, L. M.; Muller, D. A.; Guo, J.; Kim, P.; Hone, J.; Shepard, K. L.; Dean, C. R. One-Dimensional Electrical Contact to a Two-Dimensional Material. *Science* **2013**, *342* (6158), 614–617. <https://doi.org/10.1126/science.1244358>
- (43) Lee, Y.; Hwang, J.; Zhang, F.; Cho, K. First-Principles Study of Metal-Graphene Edge Contact for Ballistic Josephson Junction. *Phys. Rev. Mater.* **2019**, *3* (6), 064801. <https://doi.org/10.1103/PhysRevMaterials.3.064801>.
- (44) Xu, H.; Han, D.; Bao, Y.; Cheng, F.; Ding, Z.; Tan, S. J. R.; Loh, K. P. Observation of Gap Opening in 1T' Phase MoS₂ Nanocrystals. *Nano Lett.* **2018**, *18* (8), 5085–5090. <https://doi.org/10.1021/acs.nanolett.8b01953>.
- (45) Liu, L.; Wu, J.; Wu, L.; Ye, M.; Liu, X.; Wang, Q.; Hou, S.; Lu, P.; Sun, L.; Zheng, J.; Xing, L.; Gu, L.; Jiang, X.; Xie, L.; Jiao, L. Phase-Selective Synthesis of 1T' MoS₂ Monolayers and Heterophase Bilayers. *Nature Materials* **2018**, *17* (12), 1108–1114. <https://doi.org/10.1038/s41563-018-0187-1>.
- (46) Li, Z.; Zhai, L.; Zhang, Q.; Zhai, W.; Li, P.; Chen, B.; Chen, C.; Yao, Y.; Ge, Y.; Yang, H.; Qiao, P.; Kang, J.; Shi, Z.; Zhang, A.; Wang, H.; Liang, J.; Liu, J.; Guan, Z.; Liao, L.; Neacșu, V. A.; Ma, C.; Chen, Y.; Zhu, Y.; Lee, C.-S.; Ma, L.; Du, Y.; Gu, L.; Li, J.-F.; Tian, Z.-Q.; Ding, F.; Zhang, H. 1T'-Transition Metal Dichalcogenide Monolayers Stabilized on 4H-Au Nanowires for Ultrasensitive SERS Detection. *Nat. Mater.* **2024**, *23* (10), 1355–1362. <https://doi.org/10.1038/s41563-024-01860-w>.
- (47) Matsuyama, K.; Chen, L.; Aso, K.; Kanahashi, K.; Nagashio, K.; Oshima, Y.; Kiriya, D. Phase Engineering of 1T'-MoS₂ via Organic Enwrapment. *J. Am. Chem. Soc.* **2025**, *147* (20), 16729–16734. <https://doi.org/10.1021/jacs.5c02099>.
- (48) Deylgat, E.; Tiwari, S.; Vandenberghe, W. G.; Sorée, B. Impact of Passivation on the Dirac Cones of 2D Topological Insulators. *J. Appl. Phys.* **2022**, *131* (23), 235101. <https://doi.org/10.1063/5.0094246>.
- (49) Stepina, N. P.; Ishchenko, D. V.; Golyashov, V. A.; Bazhenov, A. O.; Goldyreva, E. S.; Akhundov, I. O.; Tarasov, A. S.; Kokh, K. A.; Tereshchenko, O. E. Epitaxial Growth of the Bi_ySb_{2-y}Te_{3-x}Se_x 3D Topological Insulator: Physical Vapor Deposition and Molecular Beam Epitaxy. *Crystal Growth & Design* **2022**, *22* (12), 7255–7263. <https://doi.org/10.1021/acs.cgd.2c00906>.
- (50) Yan, H.; Liu, L.; Loh, L.; Chhowalla, M.; Wang, Y. Gate Dielectrics for Transistors Based on Two-Dimensional Transition Metal Dichalcogenide Semiconductors. *APL Electronic Devices* **2025**, *1* (3), 031501. <https://doi.org/10.1063/5.0275690>.

Supporting Information for

“Designing Extremely Low-Power Topological
Transistors with 1T’–MoS₂ and HZO for Cryogenic
Applications”

Yosep Park¹, Yungyeong Park², Hyeonseok Choi², Subeen Lim², and Yeonghun Lee^{1,2,3}

¹Department of Intelligent Semiconductor Engineering, Incheon National University, Incheon
22012, Republic of Korea.

²Department of Electronics Engineering, Incheon National University, Incheon 22012, Republic
of Korea.

³Research Institute for Engineering and Technology, Incheon National University, Incheon
22012, Republic of Korea.

e-mail: y.lee@inu.ac.kr

Contents

Supporting Information 1. Device parameters

Section 1-1) TIFET parameters

Section 1-2) Ferroelectric material parameter in NC-TIFETs

Supporting Information 2. Model Method in NC-TIFETs

Section 2-1) Hamiltonian-based continuum ($\mathbf{k} \cdot \mathbf{p}$) model (1T'-MoS₂)

Section 2-2) Hamiltonian-based Kane–Mele model (Pt₂HgSe₃, Stanene)

Supporting Information 3. DFT parameters of 1T'-MoS₂, Pt₂HgSe₃, and stanene

Supporting Information 4. Landau-Khalatnikov (L–K) equation to model NC-TIFETs

Supporting Information 5. Optimization of NC-TIFET channel length and width

Supporting Information 6. Model parameter fitting for DFT

Supporting Information 7. Optimization of ferroelectric thickness (t_{FE}) in NC-TIFETs in cryogenic environments

Supporting Information 8. Effects of different ferroelectric materials in NC-TIFETs.

Supporting Information 9. Output characteristics of NC-TIFETs

Supporting Information 10. Formulas for TIFET drain current equation combined with contact resistance.

Supporting Information 1. Device parameters

The TIFET (NC-TIFET) model is based on the work of Park et al¹. The device parameters presented in Sections 1-1 and 1-2 were directly extracted from our device structure.

Section 1-1) TIFETs parameters

symbol	Parameter	Value
E_C	Critical electric field point	1.3 V/Å
E_g	Channel material bandgap	43 meV
δ_p	Lowest conduction band structure energy	- 0.445 eV
δ_d	Highest conduction band structure energy ²	- 0.132 eV
m_x^d/m_0	Effective mass valence band in x-direction ²	0.92
m_x^p/m_0	Effective mass conduction band in x-direction ²	0.29
m_y^d/m_0	Effective mass valence band in y-direction ²	2.32
m_y^p/m_0	Effective mass conduction band in y-direction ²	0.48
v_1	Velocity x direction ²	0.23×10^5 m/s
v_2	Velocity y direction ²	3.383×10^5 m/s
α	material specific electrical parameter ²	0.21 eÅ
t_{ch}	1T'-MoS ₂ thickness	0.5063 nm
EOT	Equivalent oxide thickness	0.5 nm
ϵ_r	The relative permittivity of 1T'-MoS ₂	2.4547

ϵ_{ox}	The relative permittivity of oxide	3.9
-----------------	------------------------------------	-----

Table S1. Summary of calculated TIFET parameters with a 1T'-MoS₂ channel. The dielectric material is SiO₂. m_0 is the rest mass of electron.

symbol	Parameter	Value
E_C	Critical electric field point	0.7 (0.93) V/Å
E_g	Channel material bandgap	62.1 (143.3) meV
a	Lattice constant	0.467 (0.75) nm
t	Hopping	0.7 (0.2) eV
λ_{SO}	Spin-orbit coupling parameter	$35/(3\sqrt{3})$ (77.5/(3√3)) meV
α_V	Staggered potential parameter	5×10^{-12} (7×10^{-12}) eV
α_R	Rashba parameter	0 (2×10^{-12}) eV
t_{ch}	Stanene thickness	0.3229 (0.5191) nm
EOT	Equivalent oxide thickness	0.5 nm
ϵ_r	The relative permittivity of channel	1.324 (6.048)
ϵ_{ox}	The relative permittivity of oxide	3.9

Table S2. Summary of calculated TIFETs channel material parameters for stanene. Parameters for Pt₂HgSe₃ are shown in parentheses. The dielectric material is SiO₂.

Section 1-2) Ferroelectric material parameter in NC-TIFET table

symbol	Parameter	Value
α_{FE}	Ferroelectric material parameters ³	-6.8×10^8 mF ⁻¹

β_{FE}		$2.87 \times 10^9 \text{ m}^5\text{F}^{-1}\text{C}^{-2}$
$T_{\text{FE_OPT}}$	Optimized Ferroelectric thickness	17.135 nm
P_r	Remanent polarization ³	34.4 $\mu\text{C}/\text{cm}^2$
E_{CO}	Coercive field ³	1.8 MV/cm

Table S3. Summary of calculated ferroelectric material parameters for HfZrO₂ (HZO) in NC-TIFETs. The optimized ferroelectric thickness which maximizes voltage amplification, $T_{\text{FE_OPT}} = -1/2\alpha_{\text{FE}}C_{\text{ch}}$, where α_{FE} is the ferroelectric material parameter and C_{ch} is the channel capacitance (using the 1T'-MoS₂ capacitance value). $T_{\text{FE_OPT}}$ is included both top and bottom layer. Note that the ferroelectric parameters (P_r , E_{CO}) listed above were extracted from P-E hysteresis measurements conducted at a frequency of 1 kHz.

Supporting Information 2. Model Method in NC-TIFETs

Section 2-1) Hamiltonian-based continuum ($\mathbf{k} \cdot \mathbf{p}$) model (1T'-MoS₂)

To investigate the characteristics of the TIFETs with 1T'-MoS₂ channel, We employed a continuum $\mathbf{k} \cdot \mathbf{p}$ Hamiltonian and parameters derived from Das et al². In this study, the parameters α and δ_p were updated to reproduce the field-induced topological phase transition with precise consideration of charge redistribution under the electric field applied along the z direction (E_z). The $\mathbf{k} \cdot \mathbf{p}$ model were implemented using the Kwant Python package⁴.

Section 2-2) Hamiltonian-based Kane–Mele model (Pt₂HgSe₃, Stanene)

We implemented the Kane-Mele tight-binding model using the Kwant Python package⁴. For details regarding the Hamiltonian and parameters for Pt₂HgSe₃ and stanene, please refer to Park et al¹. Although Pt₂HgSe₃ was not calculated in the study by Park et al., the parameter types and extraction method used in our study are consistent with those described in their work¹.

Supporting Information 3. DFT parameters of 1T'-MoS₂, Pt₂HgSe₃, and stanene

All channel materials used in the TIFET model, First-principles calculations based on DFT^{5,6} were conducted using the pseudo-atomic orbital (PAO) based software package OpenMX^{7,8} with 220 Ry of real-space grid cutoff energy and the plane wave (PW) based software package VASP⁹⁻¹³ with 500 eV of plane-wave cutoff energy. For both codes, the exchange-correlation functional was described within the generalized gradient approximation (GGA) as formulated by Perdew, Burke, and Ernzerhof (PBE)¹⁴. The self-consistent field (SCF) loop convergence criterion was set to 10⁻⁶ eV for both codes. 9×9×1 and 9×1×1 meshes were used for bulk and nanoribbon calculations, respectively, to sample the first Brillouin zone. Non-collinear spin texture and SOC effects were considered in all calculations. To eliminate spurious interactions between monolayers, a vacuum region exceeding 15 Å was added along the z-direction for both bulk and nanoribbon calculations. For atomic position relaxation, the force tolerance was set to 0.015 eV/Å for OpenMX and 0.01 eV/Å for VASP. The atomic positions and cell volume of the bulk unit cell were optimized while keeping the cell shape fixed.

Supporting Information 4. Landau-Khalatnikov (L-K) equation to model NC-TIFETs

The voltage drop across the ferroelectric layer in the NC-TIFET structure is modeled using the Landau–Khalatnikov (L-K) equation¹⁵, following the approach proposed in ref^{16–18},

$$V_{\text{FE}} = t_{\text{FE}}E_{\text{FE}} = 2\alpha_{\text{FE}}t_{\text{FE}}P + 4\beta_{\text{FE}}t_{\text{FE}}P^3, \quad (4)$$

where V_{FE} is the voltage drop across the ferroelectric layer, E_{FE} is the electric field within the ferroelectric material, P is polarization of the ferroelectric material, α_{FE} and β_{FE} are the ferroelectric material parameters, and t_{FE} is Ferroelectric material thickness (included both top and bottom layer). The values of α_{FE} , β_{FE} and t_{FE} are given in Supporting Information Table 3.

The polarization, P , can be approximated as the charge $Q \approx P$, where $Q = \psi_s C_{\text{ch}}$, $\psi_s = E_{\text{ch}} t_{\text{ch}}$ is surface potential of channel, C_{ch} is channel capacitance, E_{ch} is channel electric field, and t_{ch} is channel thickness.

From series connection of the Ferroelectric layer and topological insulator (TI) (see the small-signal model of the NC-TIFET in Figure 3c of the main text), the gate voltage is described by

$$V_{\text{G}} = V_{\text{FE}} + \psi_s = (t_{\text{ch}} + 2\alpha_{\text{FE}}t_{\text{FE}}t_{\text{ch}}C_{\text{ch}})E_{\text{ch}} + 4\beta_{\text{FE}}t_{\text{FE}}(C_{\text{ch}}t_{\text{ch}}E_{\text{ch}})^3, \quad (5)$$

Differentiating Equation (5) with respect to E_{ch} at V_{G} (i.e., $dV_{\text{G}}/dE_{\text{ch}}$ at $E_{\text{ch}} = 0$), we can obtain the optimum $t_{\text{FE}} = 1/(2\alpha_{\text{FE}}C_{\text{ch}})$, which reaches the maximum electric field condition. To satisfy t_{FE} , this maximum gate voltage condition ($V_{\text{G,max}}$) is calculated as

$$V_{\text{G,max}} = \frac{C_{\text{ch}}^2 t_{\text{ch}}^3}{P_{\text{r}}^2} E_{\text{z}}^3. \quad (6)$$

where P_{r} is remanent polarization of the ferroelectric material, which P_{r} is equal to $P_{\text{r,max}}$ in NC-TIFETs condition.

Also, from the equation (4), the P_r can be derived when the E_{FE} is zero, as expressed by

$$E_{FE} = 2\alpha_{FE}P + 4\beta_{FE}P^3 = 0, \quad (7)$$

Upon implementation as an expression for P, the following P_r is can be obtained.

$$P_r = \sqrt{-\frac{\alpha_{FE}}{2\beta_{FE}}}. \quad (8)$$

Supporting Information 5. Optimization of NC-TIFET channel length and width

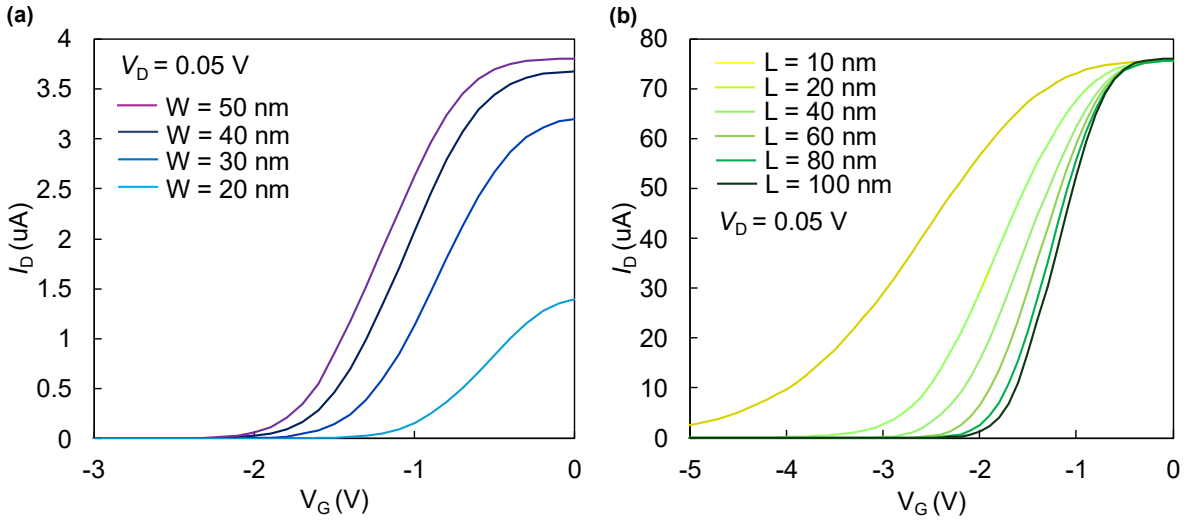


Figure S1. Effects of channel width and channel length modulation in TIFETs.

(a) Transfer characteristics as a function of channel width, ranging from 20 to 50 nm fixed at $V_D = 0.05$ V. (b) Transfer characteristics as a function of channel length, ranging from 10 to 100 nm. In Figure S1, insufficient channel width can disrupt the unique topological edge states due to the finite-size effect^{19,20}. However, this effect is suppressed as the width increases, and the device characteristics converge at a width of 50 nm, allowing the topological edge states. Additionally, an excessively short channel can induce significant tunneling leakage¹. Therefore, $W = 50$ nm and $L = 100$ nm is best transfer characteristics for the TIFETs.

Supporting Information 6. Model parameter fitting for DFT

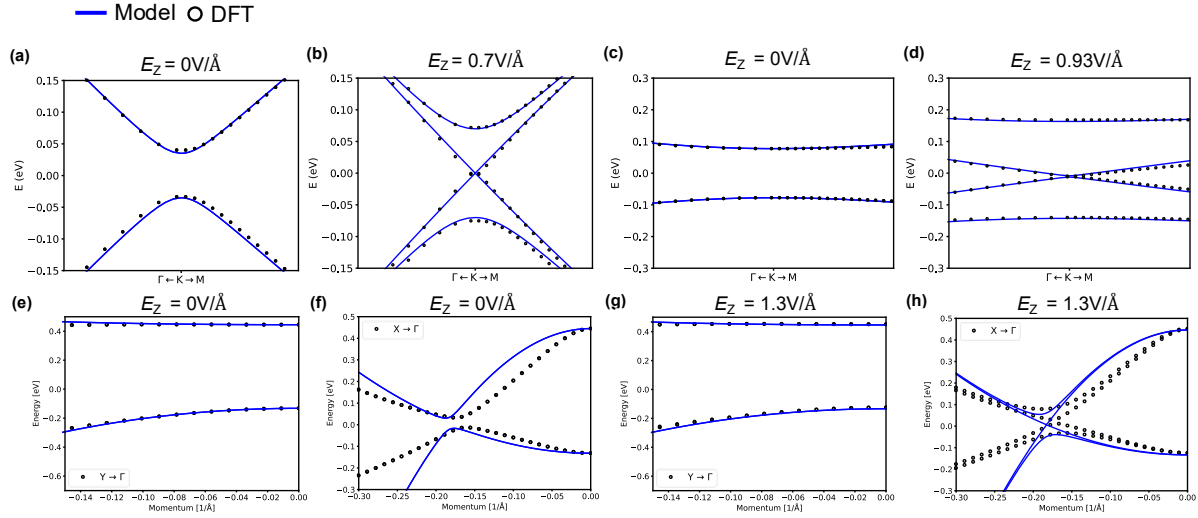


Figure S2. Parameter extraction for various topological channel materials.

(a-d) The bulk band structures of (a,b) stanene, and (c,d) Pt_2HgSe_3 have been calculated using a tight-binding (TB) model. The TB model (solid lines) is fitted to density functional theory (DFT) calculations (open circles) around K-point under different critical electric fields. (e-h) Bulk band structures of $1\text{T}'\text{-MoS}_2$, calculated using a $\mathbf{k} \cdot \mathbf{p}$ Hamiltonian. The $\mathbf{k} \cdot \mathbf{p}$ model (solid lines) is fitted to DFT calculations (open circles) along the $X\text{-}\Gamma$ and $Y\text{-}\Gamma$ high-symmetry paths. The model parameters were extracted at the ON-state ($E_z = 0 \text{ V/\AA}$) and their respective critical points ($E_z = 0.7 \text{ V/\AA}$, 0.93 V/\AA , and 1.3 V/\AA).

Supporting Information 7. Optimization of Ferroelectric thickness (t_{FE}) in NC-TIFET in cryogenic environments

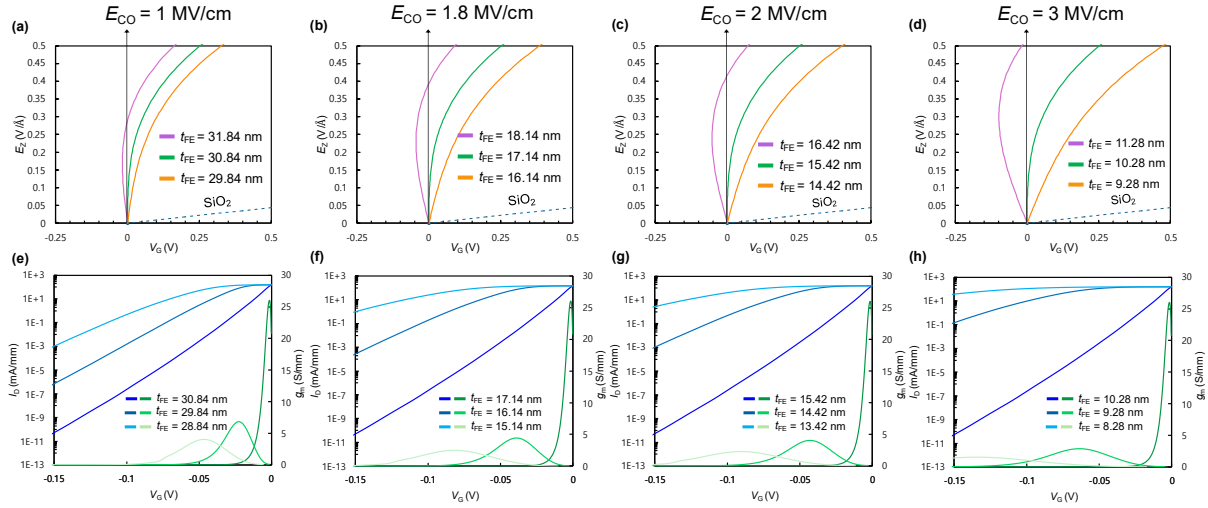


Figure S3. Effects of t_{FE} variation in NC-TIFETs under different coercive field (E_{CO}) conditions. (a-d) E_Z as a function of V_G with different t_{FE} values for $E_{CO} = 1, 1.8, 2,$ and 3 MV/cm, respectively. The dashed line represents the E_Z for a TIFET with SiO₂ gate dielectric with a thickness of 0.5 nm. (e-h) Corresponding device characteristics as a function of t_{FE} at $V_D = 0.1$ V. The left side is log-scale transfer characteristics, right side shows the linear-scale of transconductance characteristics.

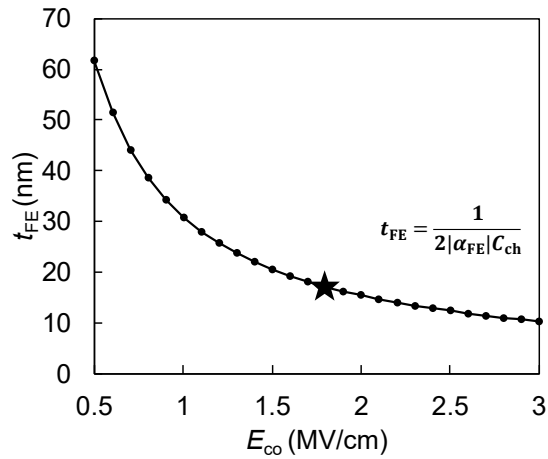


Figure S4. Optimized ferroelectric thickness ($t_{\text{FE_OPT}}$) as a function of coercive field (E_{co}). The remanent polarization (P_r) is fixed at the HZO value of $34.4 \mu\text{C}/\text{cm}^2$. The star symbol indicates the parameter used for our NC-TIFET simulation ($E_{\text{co}} = 1.8 \text{ MV}/\text{cm}$).

Optimized ferroelectric thickness $t_{\text{FE_OPT}} = 1/2\alpha_{\text{FE}}C_{\text{ch}}$ in NC-TIFETs is critical because it governs the amplification of electric field within the ferroelectric layer. As shown in Figure S3(a-d), if the thickness exceeds the optimal range, it can lead to hysteresis. Conversely, if the thickness falls short of the optimal range, it cannot achieve sufficient negative capacitance (NC) effects. As shown in Figure S3(e-h), These electric field amplification characteristics directly impact the steepness of the switching characteristics in NC-TIFETs. Also, these figure illustrates how the device characteristics ($I_{\text{D}} - V_{\text{G}}$ and g_m) evolve as E_c varies, highlighting that a thinner ferroelectric layer is required at cryogenic temperatures to maintain the non-hysteretic steep switching performance.

In cryogenic environments, the coercive field (E_{co}) of the ferroelectric layer is known to increase compared to room temperature^{21,22}. As shown in Figure S3 and S4, an increase in E_{co} (with fixed HZO P_r) leads to a larger magnitude of the ferroelectric coefficient $|\alpha_{\text{FE}}|$, since $|\alpha_{\text{FE}}| \propto E_{\text{co}}/P_r$. Consequently, the optimal thickness ($t_{\text{FE_OPT}} = 1/(2|\alpha_{\text{FE}}|C_{\text{ch}})$) required to maximize voltage gain without hysteresis decreases as the temperature drops. Consequently, the device performance becomes more sensitive to variations in ferroelectric thickness as E_{co} increases.

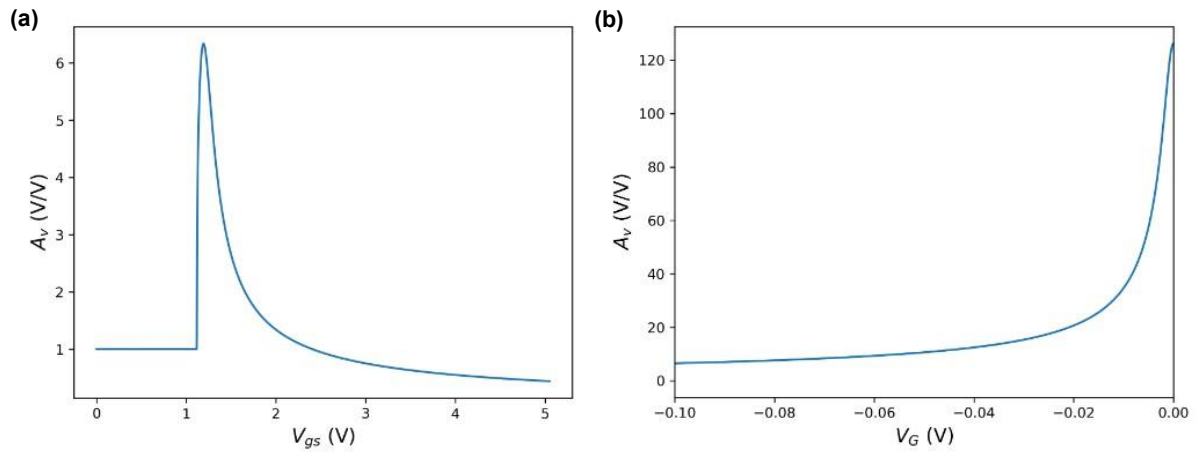


Figure S5. 2D cross-sectional plots (A_V vs V_G) of the manuscript of Figure 3. (a) Left figure is NCFET, and (b) right figure is NC-TIFET.

Supporting Information 8. Difference of ferroelectric material in NC-TIFETs.

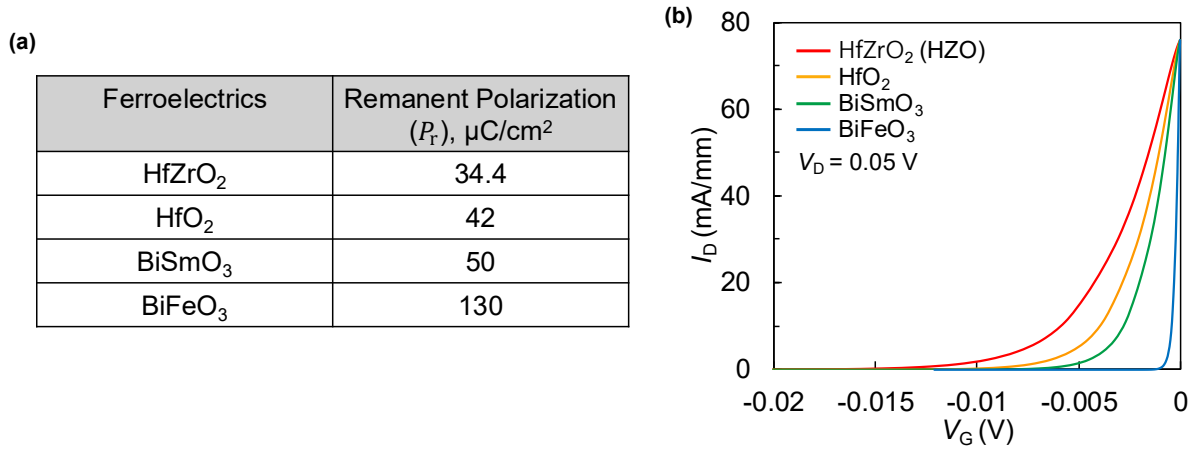


Figure S6. Impact of Remanent Polarization on Switching Characteristics. (a) Comparison of remanent polarization (P_r) for various ferroelectric materials: HfZrO₂ (HZO)³, HfO₂²³, BiSmO₃²⁴, and BiFeO₃ (BFO)²⁵. (b) Transfer characteristics of NC-TIFETs utilizing different ferroelectrics materials. For all simulations, 1T'-MoS₂ was used as the channel material. Note that all of the ferroelectric parameters are at room temperature.

A larger P_r leads to higher amplification, resulting in a steeper slope of transfer characteristics. Among the materials investigated, BiFeO₃ (BFO) exhibits the steepest switching behavior, making it particularly promising candidate for extremely low power applications.

Supporting Information 9. Output characteristics of NC-TIFETs

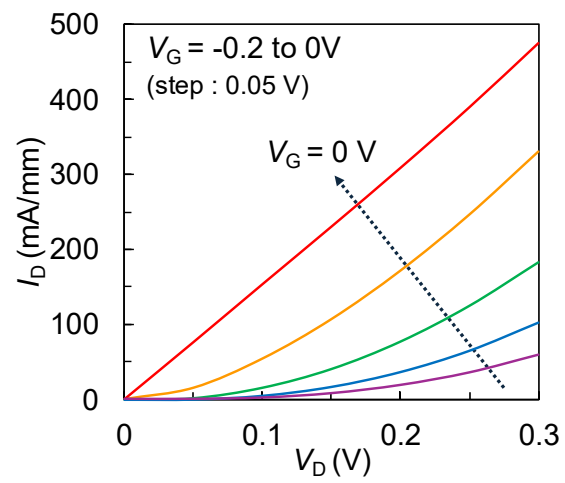


Figure S7. Output characteristics of NC-TIFETs with different V_G . Ferroelectric material is HZO and channel material is 1T'-MoS₂.

Supporting Information 10. Formulas for TIFET drain current equation combined with contact resistance.

In this study, the TIFET was modeled as a two-terminal device, where the drain current (I_D) is determined by the series combination of two primary resistance components: the contact resistance (R_C) at the source and drain, and the intrinsic channel resistance (R_{CH}). The total resistance of the device (R_{tot}) is the sum of these components (i.e., $R_{tot} = 2R_C + R_{CH}$)²⁶. Therefore, the total resistance of the TIFET was modeled as $R_{tot} = 2R_C + R_{CH} = 2R_C + 1/G_0$, where $G_0 = 2e^2/h$ is the quantum conductance. Furthermore, to incorporate the voltage drop induced by the R_C , intrinsic supply voltage (V'_D) is calculated as $V'_D = V_D - 2R_C I_D$ ²⁷, where V_D is the supply voltage.

According to Ohm's law, the I_D is the V'_D divided by the R_{tot} :

$$I'_D = \frac{V'_D}{R_{tot}} = \frac{V_D - 2R_C I_D}{2R_C + 1/G_0} \quad (9)$$

To solve for I_D , equation (9) is expressed as equation (10):

$$I'_D = \frac{V_D}{4R_C + 1/G_0} \quad (10)$$

In the case of gate-dependent transport in TIFETs, where the channel conductance $G(V_G) = I_D(V_G)/V_D$ is a function of gate bias, the expression for the drain current with contact resistance is given by equation (11):

$$I''_D = \frac{V_D}{4R_C + \frac{1}{G(V_G)}} \quad (11)$$

The transfer characteristics calculated using equation (11) are illustrated in Figure S8.

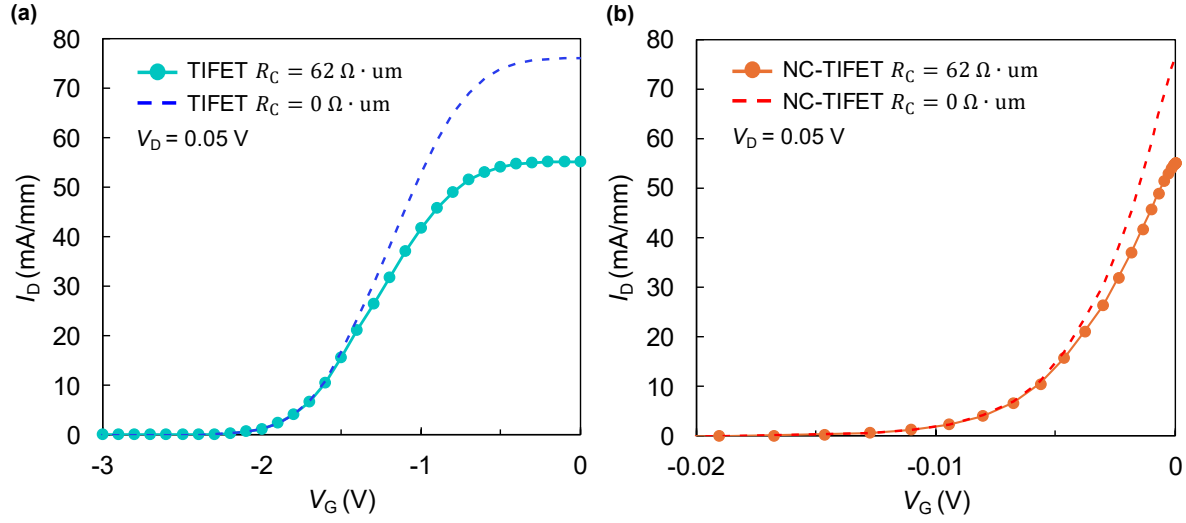


Figure S8. Impact of contact resistance (R_C) on the transfer characteristics of (a) TIFET and (b) NC-TIFET at $V_D = 0.05$ V. The dashed lines represent the ideal case without contact resistance ($R_C = 0 \Omega \cdot \mu\text{m}$), while the solid lines with symbols represent the realistic case with an optimized contact resistance of $R_C = 62 \Omega \cdot \mu\text{m}$, as reported R_C for InSe contacts²⁷. Note that the TIFET employs a SiO_2 dielectric with a $1\text{T}'\text{-MoS}_2$ channel, whereas the NC-TIFET utilizes an HZO ferroelectric with a $1\text{T}'\text{-MoS}_2$ channel.

Note that contact resistance ($R_c = 62 \Omega \cdot \mu\text{m}$) is adopted from experimental demonstrations of ohmic contacts²⁵. This assumption of ohmic contact is critical for minimizing contact resistance at cryogenic temperatures where thermionic emission is suppressed. Quantitatively, for the simulated device width of $W = 50\text{nm}$, the total series contact resistance is estimated to be $\frac{2R_C}{W} \approx 2.48 \text{ k}\Omega$.

This value is notably smaller than the quantized resistance of the 1D helical edge states ($R_{edge} = \frac{h}{2e^2} \sim 12.9 \text{ k}\Omega$). This comparison confirms that the total device resistance is dominated by the intrinsic topological edge channels rather than the contacts, preserving the ballistic transport characteristics essential for the proposed NC-TIFET operation.

As shown in Figure S8(a), the inclusion of R_C leads to a noticeable degradation in the On-current for standard TIFETs. However, for NC-TIFETs, as shown in Figure S8(b), even when accounting for a realistic $R_C = 62 \text{ } \Omega \cdot \mu\text{m}$, the NC effect effectively preserves the steep switching slope. Although the On-current is slightly reduced compared to the ideal case, the voltage gain and switching capability remain robust, confirming the device's potential for high-performance applications.

Reference

- (1) Park, Y., Park, H., Choi, S., Lim, D., Kim, Y. & Lee, Y. Tight-Binding Device Modeling of 2-D Topological Insulator Field-Effect Transistors with Gate-Induced Phase Transition. *IEEE Trans. Electron Devices* **71**, 5739–5743 (2024). <https://doi.org/10.1109/Ted.2024.3427091>.
- (2) Das, B.; Sen, D.; Mahapatra, S. Tuneable Quantum Spin Hall States in Confined 1T' Transition Metal Dichalcogenides. *Sci Rep* **2020**, *10* (1), 6670. <https://doi.org/10.1038/s41598-020-63450-5>.
- (3) Zacharaki, C.; Tsipas, P.; Chaitoglou, S.; Fragkos, S.; Axiotis, M.; Lagoyiannis, A.; Negrea, R.; Pintilie, L.; Dimoulas, A. Very Large Remanent Polarization in Ferroelectric Hf1-xZrxO2 Grown on Ge Substrates by Plasma Assisted Atomic Oxygen Deposition. *Appl. Phys. Lett.* **2019**, *114* (11), 112901. <https://doi.org/10.1063/1.5090036>.
- (4) Groth, C. W.; Wimmer, M.; Akhmerov, A. R.; Waintal, X. Kwant: A Software Package for Quantum Transport. *New J. Phys.* **2014**, *16* (6), 063065. <https://doi.org/10.1088/1367-2630/16/6/063065>.
- (5) Kohn, W.; Sham, L. J. Self-Consistent Equations Including Exchange and Correlation Effects. *Phys. Rev.* **1965**, *140* (4A), A1133–A1138. <https://doi.org/10.1103/PhysRev.140.A1133>.
- (6) Hohenberg, P.; Kohn, W. Inhomogeneous Electron Gas. *Phys. Rev.* **1964**, *136* (3B), B864–B871. <https://doi.org/10.1103/PhysRev.136.B864>.
- (7) Ozaki, T. Variationally Optimized Atomic Orbitals for Large-Scale Electronic Structures. *Phys. Rev. B* **2003**, *67* (15), 155108. <https://doi.org/10.1103/PhysRevB.67.155108>.
- (8) Ozaki, T.; Kino, H. Numerical Atomic Basis Orbitals from H to Kr. *Phys. Rev. B* **2004**, *69* (19), 195113. <https://doi.org/10.1103/PhysRevB.69.195113>.
- (9) Kresse, G.; Hafner, J. Norm-Conserving and Ultrasoft Pseudopotentials for First-Row and Transition Elements. *J. Phys.: Condens. Matter* **1994**, *6* (40), 8245–8257. <https://doi.org/10.1088/0953-8984/6/40/015>.
- (10) Kresse, G.; Furthmüller, J. Efficiency of Ab-Initio Total Energy Calculations for Metals and Semiconductors Using a Plane-Wave Basis Set. *Computational Materials Science* **1996**, *6* (1), 15–50. [https://doi.org/10.1016/0927-0256\(96\)00008-0](https://doi.org/10.1016/0927-0256(96)00008-0).
- (11) Kresse, G.; Furthmüller, J. Efficient Iterative Schemes for Ab Initio Total-Energy Calculations Using a Plane-Wave Basis Set. *Phys. Rev. B* **1996**, *54* (16), 11169–11186. <https://doi.org/10.1103/PhysRevB.54.11169>.

- (12) Kresse, G.; Hafner, J. *Ab Initio* Molecular Dynamics for Liquid Metals. *Phys. Rev. B* **1993**, *47* (1), 558–561. <https://doi.org/10.1103/PhysRevB.47.558>.
- (13) Kresse, G.; Joubert, D. From ultrasoft pseudopotentials to the projector augmented-wave method. *Phys. Rev. B* **1999**, *59* (3), 1758–1775. <https://doi.org/10.1103/PhysRevB.59.1758>.
- (14) Perdew, J. P.; Burke, K.; Ernzerhof, M. Generalized Gradient Approximation Made Simple. *Phys. Rev. Lett.* **1996**, *77* (18), 3865–3868. <https://doi.org/10.1103/PhysRevLett.77.3865>.
- (15) Landau, L. D.; Khalatnikov, I. M. On the Anomalous Absorption of Sound near a Second Order Phase Transition Point. In *Dokl. Akad. Nauk SSSR*; 1954; Vol. 96, p 25.
- (16) Park, Y.; Lee, H.; Lee, Y. Trap-Enhanced Steep-Slope Negative-Capacitance FETs Using Amorphous Oxide Semiconductors. *ACS Appl. Electron. Mater.* **2025**, *7* (12), 5705–5711. <https://doi.org/10.1021/acsaelm.5c00767>.
- (17) You, W.-X.; Su, P. Intrinsic Difference Between 2-D Negative-Capacitance FETs With Semiconductor-on-Insulator and Double-Gate Structures. *IEEE Transactions on Electron Devices* **2018**, *65* (10), 4196–4201. <https://doi.org/10.1109/TED.2018.2866125>.
- (18) Fuhrer, M. S.; Edmonds, M. T.; Culcer, D.; Nadeem, M.; Wang, X.; Medhekar, N.; Yin, Y.; Cole, J. H. Proposal for a Negative Capacitance Topological Quantum Field-Effect Transistor. In *2021 IEEE International Electron Devices Meeting (IEDM)*; 2021; p 38.2.1-38.2.4. <https://doi.org/10.1109/IEDM19574.2021.9720587>.
- (19) Nadeem, M.; Zhang, C.; Culcer, D.; Hamilton, A. R.; Fuhrer, M. S.; Wang, X. Optimizing Topological Switching in Confined 2D-Xene Nanoribbons via Finite-Size Effects. *Applied Physics Reviews* **2022**, *9* (1), 011411. <https://doi.org/10.1063/5.0076625>.
- (20) Pournaghavi, N.; Sadhukhan, B.; Delin, A. Spin Transport Properties in a Topological Insulator Sandwiched between Two-Dimensional Magnetic Layers. *Scientific Reports* **2025**, *15* (1), 2255. <https://doi.org/10.1038/s41598-024-80694-7>.
- (21) Bohuslavskiy, H.; Grigoras, K.; Ribeiro, M.; Prunnila, M.; Majumdar, S. Ferroelectric Hf_{0.5}Zr_{0.5}O₂ for Analog Memory and In-Memory Computing Applications Down to Deep Cryogenic Temperatures. *Advanced Electronic Materials* **2024**, *10* (7), 2300879. <https://doi.org/10.1002/aelm.202300879>.
- (22) Ram, M. K.; Wernersson, L.-E. Cryogenic Ferroelectricity of HZO With an Aluminum Oxide Interlayer. *IEEE Transactions on Electron Devices* **2026**, *73* (1), 652–658. <https://doi.org/10.1109/TED.2025.3629590>.
- (23) Schenk, T.; Fancher, C. M.; Park, M. H.; Richter, C.; Künne, C.; Kersch, A.; Jones, J. L.; Mikolajick, T.; Schroeder, U. On the Origin of the Large Remanent Polarization in La:HfO₂. *Advanced Electronic Materials* **2019**, *5* (12), 1900303. <https://doi.org/10.1002/aelm.201900303>.
- (24) Yang, Q.; Hu, J.; Fang, Y.-W.; Jia, Y.; Yang, R.; Deng, S.; Lu, Y.; Dieguez, O.; Fan, L.; Zheng, D.; Zhang, X.; Dong, Y.; Luo, Z.; Wang, Z.; Wang, H.; Sui, M.; Xing, X.; Chen, J.; Tian, J.; Zhang, L. Ferroelectricity in Layered Bismuth Oxide down to 1 Nanometer. *Science* **2023**, *379* (6638), 1218–1224. <https://doi.org/10.1126/science.abm5134>.
- (25) Zhang, J. X.; He, Q.; Trassin, M.; Luo, W.; Yi, D.; Rossell, M. D.; Yu, P.; You, L.; Wang, C. H.; Kuo, C. Y.; Heron, J. T.; Hu, Z.; Zeches, R. J.; Lin, H. J.; Tanaka, A.; Chen, C. T.; Tjeng, L. H.; Chu, Y.-H.; Ramesh, R. Microscopic Origin of the Giant Ferroelectric Polarization in Tetragonal-like BiFeO_3 . *Phys. Rev. Lett.* **2011**, *107* (14), 147602. <https://doi.org/10.1103/PhysRevLett.107.147602>.
- (26) Shen, P.-C.; Su, C.; Lin, Y.; Chou, A.-S.; Cheng, C.-C.; Park, J.-H.; Chiu, M.-H.; Lu, A.-Y.; Tang, H.-L.; Tavakoli, M. M.; Pitner, G.; Ji, X.; Cai, Z.; Mao, N.; Wang, J.; Tung, V.; Li,

J.; Bokor, J.; Zettl, A.; Wu, C.-I.; Palacios, T.; Li, L.-J.; Kong, J. Ultralow Contact Resistance between Semimetal and Monolayer Semiconductors. *Nature* **2021**, *593* (7858), 211–217. <https://doi.org/10.1038/s41586-021-03472-9>.

(27) Jiang, J.; Xu, L.; Qiu, C.; Peng, L.-M. Ballistic Two-Dimensional InSe Transistors. *Nature* **2023**, *616* (7957), 470–475. <https://doi.org/10.1038/s41586-023-05819-w>.